



Entropy and heat transfer investigation of Casson–Maxwell, Casson–Jeffrey, and Casson–Oldroyd-B binary nanofluids in a parabolic trough solar collector: a comparative study

Philopatir B. Raafat¹ · Fayez N. Ibrahim¹

Received: 29 October 2022 / Accepted: 24 January 2023 / Published online: 28 February 2023
© The Author(s) 2023

Abstract

In this paper, we compared copper-engine oil Casson–Maxwell, Casson–Jeffrey, and Casson–Oldroyd-B binary nanofluids in a parabolic trough solar collector. Using appropriate similarity variables, the partial differential equations governing nanofluid flow were converted into ordinary differential equations. The resulting nonlinear systems were solved using the shooting method. The numerical results were presented in graphical and tabular forms. We investigated the effects of different parameters controlling the flow on the velocity, temperature, entropy generation, skin friction, and local Nusselt number of the nanofluids. Overall, the Casson–Maxwell and Casson–Jeffrey nanofluid models had better efficiency than the Casson–Oldroyd-B nanofluid model.

Keywords Casson · Jeffrey · Oldroyd-B · Maxwell · Parabolic trough solar collector · Binary nanofluid

List of symbols

a	Primary stretching rate
a^*	Thermal discrepancy rate
B_0	Strength of the constant magnetic field
B_K	Brinkman number
Bi_T	Thermal Biot number
C_f	Skin friction constant
C_p	Specific heat
D_T	Thermophoretic diffusion coefficient
Ec	Eckert number
e_{ij}	(i, j) Th component of the deformation rate
f'	Dimensionless velocity
h_f	Heat transfer coefficient
k	Thermal conductivity
k_p	Porosity
k^*	Mean absorption coefficient
K	Porosity parameter
m	Nanoparticle shape factor
M	Magnetic number
N_G	Entropy generation dimensionless factor

N_r	Thermal radiation parameter
N_t	Thermophoretic parameter
Nu_x	Local Nusselt number
N_w	Slip length
Pr	Prandtl number
p_y	Yield stress
Q	Heat source parameter
Q_0	Heat source
q_r	Radiative heat flux
Re	Reynolds number
Re_x	Local Reynolds number
S	Mass transfer parameter
t	Time
T	Temperature
u	v , Velocity components
V_w	Surface permeability
x, y	Dimensional space coordinates

Greek symbols

α	Thermal diffusion rate
β	Casson parameter
β_1	β_3 , Deborah numbers
$\dot{\gamma}$	Rate of strain tensor
$\tilde{\gamma}$	Upper convected derivative of the strain tensor
Γ	The magnetic field's angle of inclination
η	Dimensionless space variable
θ	Dimensionless temperature
κ_0	Surface thermal conductance

✉ Fayez N. Ibrahim
fayeznasif@yahoo.co.uk

Philopatir B. Raafat
philopatirraafat@gmail.com

¹ Faculty of Science, Department of Mathematics, Ain Shams University, Cairo, Egypt

λ_1	Fluid relaxation time
λ_2	Ratio of the relaxation to retardation times
λ_3	Fluid retardation time
Λ	Velocity parameter
μ	Viscosity
μ_0	Low-shear viscosity
μ_B	Plastic dynamic viscosity of the Casson fluid
ν	Kinematic viscosity
π_c	Critical value of the deformation rate
ρ	Density
σ	Electrical conductivity
σ^*	Stefan–Boltzmann constant
τ	Extra stress tensor
τ_{ij}	Stress tensor
$\tilde{\tau}$	Upper convected derivative of the stress tensor
φ	Nanoparticle concentration
χ	Ratio of the operative heat capability
Ω	Difference in temperature parameter

Subscripts

f	Base fluid
nf	Nanofluid
s	Solid particles
W	Wall
∞	Free stream

Introduction

In recent years, renewable energy, in general, and solar energy, in particular, have gained considerable attention owing to their environmental friendliness and effectiveness in generating electrical and thermal energy. Solar energy is usually harnessed using photovoltaic technology or solar collectors (SCs). A SC is preferable owing to its cost efficiency and energy collection capabilities [1]. The suspension of nanoparticles in the base fluid is a major advancement in developing SCs with enhanced efficiency. Choi [2] was the first to observe improved heat transfer using nanoparticles. Over the years, studies investigating nanofluids in parabolic trough solar collectors (PTSCs) have been conducted [3–6]. Shahzad et al. [7] studied the thermal characterization of a solar-powered ship using Oldroyd hybrid nanofluids in a PTSC. Jamshed et al. [8] performed a thermal examination of renewable solar energy in a PTSC using a Maxwell nanofluid. Jamshed et al. [9] conducted a computational study on implementing renewable solar energy in the presence of a Maxwell nanofluid in a PTSC. Nabwey et al. [10] investigated the effect of resistive and radiative heats on enhanced heat transfer of a PTSC using Maxwell–Oldroyd-B nanofluids.

Many researchers have studied the fractional calculus methods, the effects of convective heat transfer and thermal

radiation processes on nanofluid efficiency, and the applications of nanofluids in the presence of oxytactic microorganisms in different engineering problems [11–28].

Currently, binary nanofluids are being studied for various applications as they have better energy transfer than mono nanofluids [29–32]. Yu [33] employed a decoupled wavelet approach for multiple physical flow fields of binary nanofluids in double-diffusive convection. Lee et al. [34] conducted a theoretical study on the performance comparison of various SCs using binary nanofluids. Reddy et al. [35] studied the effects of viscous dissipation and thermal radiation on electrically conducting Casson–Carreau nanofluid flow using the Cattaneo–Christov heat flux model. Oyelakin et al. [36] investigated the effect of double-diffusion convection on three-dimensional magnetohydrodynamic (MHD) stagnation point flow of a tangent hyperbolic Casson nanofluid. Yousef et al. [37] explored the chemical reaction impact on MHD dissipative Casson–Williamson nanofluid flow over a slippery stretching sheet through a porous medium.

Jamshed and Nisar [38] compared copper/alumina-engine oil Williamson nanofluids in a PTSC. They concluded that copper was considerably better than alumina in terms of heat transfer. Other studies [39–41] have also suggested the use of copper rather than other materials owing to its high efficiency to achieve enhanced thermal properties. Notably, the shape of nanoparticles can affect nanofluid heat transfer ability [42, 43].

Based on the literature review, we believe that a direct comparison of binary nanofluids in PTSCs is lacking, and we hope to contribute toward mitigating this lack of knowledge. Notably, the Jeffrey and Casson–Jeffrey nanofluid models have not been investigated in PTSC settings. The other novel aspects of the current study are as follows:

- The comparison between the Casson–Maxwell, Casson–Jeffrey, and Casson–Oldroyd-B binary nanofluids in PTSCs.
- The consideration of thermophoretic diffusivity.
- The consideration of a constant inclined magnetic field.
- The consideration of different nanoparticle shapes.

The practical significance of this study lies in the use of the considered models in PTSCs [10, 41, 44], solar water pumps [45], and solar-powered ships [7, 8].

Formulation of the problem

Consider the velocity and temperature of a nonuniform stretching insulated sheet as follows [46]:

$$U_W(x, 0) = ax, T_W(x, 0) = T_\infty + a^*x \quad (1)$$

where a , a^* , T_W , and T_∞ denote the primary stretching rate, thermal discrepancy rate, heat at the wall, and heat at the

free stream, respectively. Figure 1 presents a schematic of a PTSC.

Stress tensor of binary fluids

Herein, we studied three binary liquids: Casson–Maxwell, Casson–Jeffrey, and Casson–Oldroyd-B.

The rheological equation of state of an incompressible and isotropic flow of a Casson fluid is as follows [47]:

$$\tau_{ij} = \begin{cases} 2\left(\mu_B + \frac{p_y}{\sqrt{2\pi}}\right)e_{ij}, & \pi > \pi_c \\ 2\left(\mu_B + \frac{p_y}{\sqrt{2\pi_c}}\right)e_{ij}, & \pi < \pi_c \end{cases} \quad (2)$$

where τ_{ij} denotes the stress tensor, e_{ij} denotes the (i, j) th component of the deformation rate, $\pi = e_{ij}e_{ij}$, i.e., the product of the component of deformation with itself, π_c denotes a critical value of this product based on the non-Newtonian model, μ_B denotes the plastic dynamic viscosity of the Casson fluid, and p_y denotes the yield stress of the fluid.

The Maxwell model is a simple linear model with one elastic parameter, which is λ_1 , the fluid relaxation time. This model combines the concepts of fluid viscosity and solid elasticity to arrive at the following relation:

$$\tau + \lambda_1 \frac{\partial \tau}{\partial t} = \mu_0 \dot{\gamma} \quad (3)$$

The Jeffrey model extends the Maxwell model by adding a time derivative of the strain rate to yield the following equation:

$$\tau + \lambda_1 \frac{\partial \tau}{\partial t} = \mu_0 \left(\dot{\gamma} + \lambda_3 \frac{\partial \dot{\gamma}}{\partial t} \right) \quad (4)$$

where λ_3 denotes the retardation time, which is a measure of the time required by the material to respond to deformation.

The Oldroyd-B model is the nonlinear equivalent of the linear Jeffrey model, because it considers the frame invariance in the nonlinear regime. It can be constructed by replacing the partial time derivatives in the differential form of the Jeffrey model with the upper convective time derivatives to achieve the following form:

$$\tau + \lambda_1 \tilde{\tau} = \mu_0 (\dot{\gamma} + \lambda_3 \tilde{\dot{\gamma}}) \quad (5)$$

where $\tilde{\tau}$ and $\tilde{\dot{\gamma}}$ denote the upper convected derivatives of the stress and strain tensors, respectively, and are expressed as follows:

$$\tilde{\tau} = \frac{\partial \tau}{\partial t} + \mathbf{v} \cdot \nabla \tau - (\nabla \mathbf{v})^T \cdot \tau - \tau \cdot \nabla \mathbf{v} \quad (6)$$

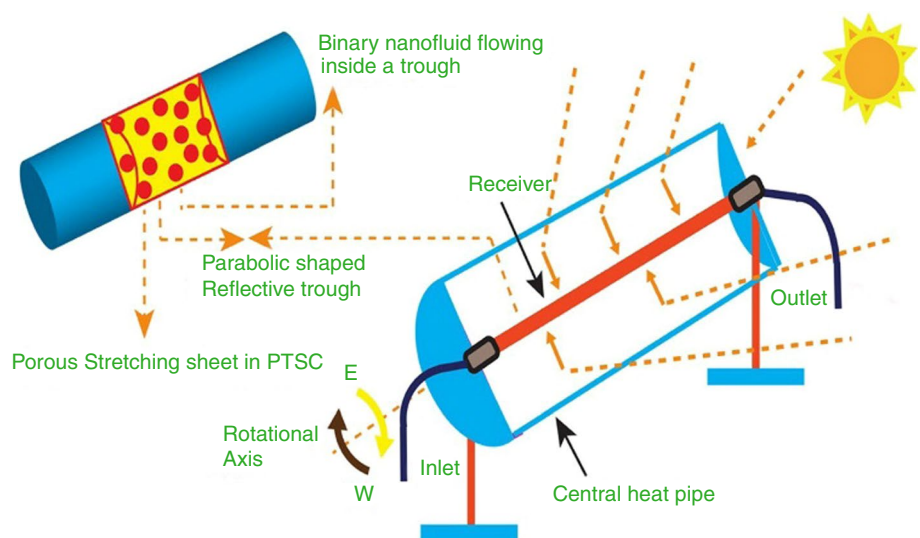
$$\tilde{\dot{\gamma}} = \frac{\partial \dot{\gamma}}{\partial t} + \mathbf{v} \cdot \nabla \dot{\gamma} - (\nabla \mathbf{v})^T \cdot \dot{\gamma} - \dot{\gamma} \cdot \nabla \mathbf{v} \quad (7)$$

For more details about the different aspects of various non-Newtonian fluids we refer the reader to the comprehensive work conducted by Sochi [48].

Governing equations

The principles of conservation of mass, momentum, and energy are applied to two-dimensional, incompressible, laminar, steady flow of binary nanofluids. We also consider the porous medium along with the thermophoresis effect and a constant inclined magnetic field as follows [44, 49]:

Fig. 1 Schematic of a parabolic trough solar collector (PTSC). Reprinted with alterations under Creative Common CC BY licence from [52]



$$\frac{\partial u}{\partial x} + \frac{\partial v}{\partial y} = 0 \tag{8}$$

$$\begin{aligned} u \frac{\partial u}{\partial x} + v \frac{\partial u}{\partial y} = & -\lambda_1 \left(u^2 \frac{\partial^2 u}{\partial x^2} + v^2 \frac{\partial^2 u}{\partial y^2} + 2uv \frac{\partial^2 u}{\partial x \partial y} \right) \\ & + \frac{\mu_{nf}}{\rho_{nf}(1 + \lambda_2)} \left(\left(1 + \frac{1}{\beta} \right) \frac{\partial^2 u}{\partial y^2} \right. \\ & \left. + \lambda_3 \left(u \frac{\partial^3 u}{\partial x \partial y^2} + \frac{\partial u}{\partial y} \frac{\partial^2 u}{\partial x \partial y} + v \frac{\partial^3 u}{\partial y^3} - \frac{\partial u}{\partial x} \frac{\partial^2 u}{\partial y^2} \right) \right) \\ & - \frac{\mu_{nf}}{\rho_{nf} k_p} u - \frac{\sigma_{nf} B_0^2}{\rho_{nf}} u \sin^2(\Gamma) \end{aligned} \tag{9}$$

$$\begin{aligned} u \frac{\partial T}{\partial x} + v \frac{\partial T}{\partial y} = & \frac{k_{nf}}{(\rho C_p)_{nf}} \frac{\partial^2 T}{\partial y^2} + \frac{Q_0}{(\rho C_p)_{nf}} (T - T_\infty) \\ & + \frac{\mu_{nf}}{(\rho C_p)_{nf}} \left(\frac{\partial u}{\partial y} \right)^2 - \frac{1}{(\rho C_p)_{nf}} \frac{\partial q_r}{\partial y} \\ & + \chi \left[\frac{D_T}{T_\infty} \left(\frac{\partial T}{\partial y} \right)^2 \right] + \frac{\sigma_{nf} B_0^2}{(\rho C_p)_{nf}} u^2 \sin^2(\Gamma) \end{aligned} \tag{10}$$

The suitable boundary constraints are as follows:

$$u = U_w + N_w \frac{\partial u}{\partial y}, v = V_w, \kappa_0 \frac{\partial T}{\partial y} = -h_f(T_w - T) \quad \text{at } y = 0 \tag{11}$$

$$u \rightarrow 0, T \rightarrow T_\infty \quad \text{as } y \rightarrow \infty \tag{12}$$

where u and v denote the velocity components in the x and y directions, respectively; μ_{nf} , ρ_{nf} , σ_{nf} , k_{nf} , and $C_{p,nf}$ denote the nanofluid viscosity, density, electrical conductivity,

thermal conductivity, and specific heat, respectively; λ_2 denotes the ratio of the relaxation to retardation times; β denotes the Casson parameter; k_p denotes the porosity; B_0 denotes the strength of the magnetic field perpendicular to \overline{OH} , and Γ denotes the angle of inclination of the magnetic field; T denotes the nanofluid temperature; Q_0 denotes the heat source; q_r denotes the radiative heat flux; χ denotes the ratio of operative heat capability; D_T denotes the thermophoresis diffusion coefficient; N_w denotes the slip length; V_w denotes the surface permeability; κ_0 denotes the surface thermal conductance; and h_f denotes the heat transfer coefficient. Figure 2 presents the boundary layer flow in a PTSC.

The following conditions describe the different case studies:

- (1) $\lambda_1 \neq 0, \lambda_2 = 0, \lambda_3 = 0$ represents the Casson–Maxwell model.
- (2) $\lambda_1 = 0, \lambda_2 \neq 0, \lambda_3 \neq 0$ represents the Casson–Jeffrey model.
- (3) $\lambda_1 \neq 0, \lambda_2 = 0, \lambda_3 \neq 0$ represents the Casson–Oldroyd-B model.

The radiative heat flux under the Rosseland approximation [21, 50] takes the form $q_r = -\frac{16\sigma^* T_\infty^3}{3k^*} \frac{\partial T}{\partial y}$ in which σ^* is the Stefan–Boltzmann constant and k^* is the mean absorption coefficient.

Table 1 presents the thermophysical aspects of the nanofluids [7, 51], Table 2 specifies the nanoparticle shape factor (m) values for various particle shapes [52, 53], and Table 3 lists the substance properties of engine oil and copper [52].

Fig. 2 PTSC inner geometry. Reprinted with alterations under Creative Common CC BY licence from [7]

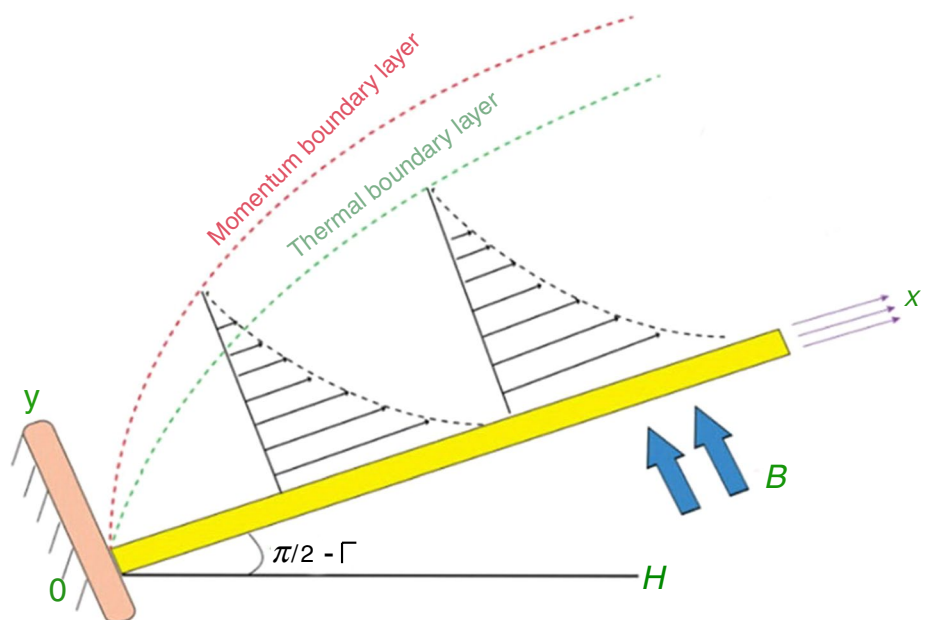


Table 1 Thermophysical features of nanofluids

Feature	Nanofluid
Viscosity	$\frac{\mu_{nf}}{\mu_f} = \frac{1}{(1-\varphi)^{2.5}} = \frac{1}{\varphi_1}$
Density	$\frac{\rho_{nf}}{\rho_f} = \left(1 - \varphi + \varphi \frac{\rho_s}{\rho_f}\right) = \varphi_2$
Heat capacity	$\frac{(\rho C_p)_{nf}}{(\rho C_p)_f} = \left(1 - \varphi + \varphi \frac{(\rho C_p)_s}{(\rho C_p)_f}\right) = \varphi_3$
Electrical conductivity	$\frac{\sigma_{nf}}{\sigma_f} = \left(1 + \frac{3\left(\frac{\sigma_s}{\sigma_f} - 1\right)\varphi}{\left(\frac{\sigma_s}{\sigma_f} + 2\right) - \left(\frac{\sigma_s}{\sigma_f} - 1\right)\varphi}\right) = \varphi_4$
Thermal conductivity	$\frac{k_{nf}}{k_f} = \left(\frac{(k_s + (m-1)k_f) - (m-1)\varphi(k_f - k_s)}{(k_s + (m-1)k_f) + \varphi(k_f - k_s)}\right) = \varphi_5$

Table 2 Shape factor values






Nanoparticle type	Shape	Shape factor (<i>m</i>)
Sphere		3
Hexahedron		3.7221
Tetrahedron		4.0613
Column		6.3698
Lamina		16.1576

Table 3 Material specifications at 20 °C

Material	$\rho/\text{kg m}^{-3}$	$C_p/\text{J kg}^{-1} \text{K}^{-1}$	$k/\text{W m}^{-1} \text{K}^{-1}$	$\sigma/\text{S m}^{-1}$
Engine oil	884	1910	0.144	0.125×10^{-11}
Copper	8933	385	401	5.96×10^7

Solution of the problem

To transform the partial differential equations to ordinary differential equations (ODEs), we introduce the following similarity variables [44]:

$$u = axf'(\eta), v = -\sqrt{av}f(\eta), \theta(\eta) = \frac{T - T_\infty}{T_w - T_\infty}, \eta = y\sqrt{\frac{a}{v}} \tag{13}$$

This transforms Eqs. (9–10) along with boundary conditions (11–12) to the following forms:

$$ff'' - \beta_1(f^2f'' - 2ff'f''') + \frac{1}{\varphi_1\varphi_2(1 + \lambda_2)} \left(\left(1 + \frac{1}{\beta}\right) f'''' + \beta_3(f''^2 - ff''''') \right) - \frac{K}{\varphi_1\varphi_2} f' - M \frac{\varphi_4}{\varphi_2} f' \sin^2(\Gamma) - f'^2 = 0 \tag{20}$$

$$\left(\frac{\varphi_5}{\text{Pr}} + N_t\right)\theta'' + \varphi_3f\theta' + Q\theta + \frac{\text{Ec}}{\varphi_1}f''^2 + N_t\varphi_3\theta'^2 + \varphi_4ME\text{csin}^2(\Gamma)f'^2 = 0 \tag{15}$$

$$f'(0) = 1 + \Lambda f''(0), f(0) = S, \theta'(0) = -\text{Bi}_T(1 - \theta(0)) \tag{16}$$

$$f'(\eta) \rightarrow 0, \theta(\eta) \rightarrow 0 \text{ as } \eta \rightarrow \infty \tag{17}$$

where $\beta_1 = \lambda_1 a$ and $\beta_3 = \lambda_3 a$ denote Deborah numbers, $K = \frac{\mu_f}{a\rho_f k_p}$ denotes the porosity parameter, $M = \frac{\sigma_f B_0^2}{a\rho_f}$ denotes the magnetic number, $\alpha = \frac{k_f}{(\rho C_p)_f}$ denotes the thermal diffusion rate, $\nu = \frac{\mu_f}{\rho_f}$ denotes the kinematic viscosity, $\text{Pr} = \frac{\nu}{\alpha}$ denotes the Prandtl number, $N_t = \frac{16\sigma^* T_\infty^3}{3k^* \nu (\rho C_p)_f}$ denotes the thermal radiation parameter, $Q = \frac{Q_0}{a(\rho C_p)_f}$ denotes the heat source parameter, $\text{Ec} = \frac{U_w^2}{C_{pf}(T_w - T_\infty)}$ denotes the Eckert number, $N_t = \frac{\chi D_T (T_w - T_\infty)}{\nu T_\infty}$ denotes the thermophoretic parameter, $\Lambda = N_w \sqrt{\frac{a}{\nu}}$ denotes the velocity slip parameter, $S = -V_w \sqrt{\frac{1}{\nu a}}$ denotes the mass transfer parameter, and $\text{Bi}_T = \frac{h_f}{\kappa_0} \sqrt{\frac{\nu}{a}}$ denotes the thermal Biot number.

Physiological concepts of interest

Considerable attention is directed toward the skin friction constant C_f , the local Nusselt number Nu_x , and the entropy generation equation [45, 46, 52, 54]:

$$C_f = \frac{\tau_w}{\rho_f U_w^2}, Nu_x = \frac{xq_w}{k_f(T_w - T_\infty)} \tag{18}$$

$$E_G = \frac{k_{nf}}{T_\infty^2} \left(\left(\frac{\partial T}{\partial y}\right)^2 + \frac{16}{3} \frac{\sigma^* T_\infty^3}{k^* \nu (\rho C_p)_f} \left(\frac{\partial T}{\partial y}\right)^2 \right) + \frac{\mu_{nf}}{T_\infty} \left(\frac{\partial u}{\partial y}\right)^2 \left(1 + \frac{1}{\beta}\right) + \frac{\mu_{nf} u^2}{k_p T_\infty} + \frac{\sigma_{nf} B_0^2}{T_\infty} u^2 \sin^2(\Gamma) \tag{19}$$

where

$$\tau_w = \mu_{nf} \frac{\left(1 + \frac{1}{\beta}\right)}{\left(1 + \lambda_2\right)} \left(\frac{\partial u}{\partial y}\right)_{y=0} \text{ and } q_w = -k_{nf} \left(1 + \frac{16}{3} \frac{\sigma^* T_\infty^3}{k^* \nu (\rho C_p)_f}\right) \left(\frac{\partial T}{\partial y}\right)_{y=0} \tag{14}$$

Using the dimensionless parameters defined in Eq. (13), we get the following:

$$C_f Re_x^{\frac{1}{2}} = \frac{\left(1 + \frac{1}{\beta}\right)}{(1 + \lambda_2)\varphi_1} f''(0), \quad Nu_x Re_x^{-\frac{1}{2}} = -(1 + N_r)\varphi_5 \theta'(0) \tag{21}$$

$$N_G = Re \left[\varphi_5 (1 + N_r) \theta'^2 + \frac{B_K}{\varphi_1 \Omega} \left(\left(1 + \frac{1}{\beta}\right) f''^2 + K f'^2 + M \varphi_1 \varphi_4 \sin^2(\Gamma) f'^2 \right) \right] \tag{22}$$

where $Re_x = \frac{xU_w}{\nu}$ denotes the local Reynolds number depending on the stretching velocity, $N_G = \frac{E_G T_\infty^2 a^2}{k_f(T_w - T_\infty)^2}$ denotes the entropy generation dimensionless factor, $Re = \frac{U_w a^2}{\nu x}$ denotes the Reynolds number, $\Omega = \frac{(T_w - T_\infty)}{T_\infty}$ denotes difference in temperature parameter, and $B_K = \frac{\mu_f U_w^2}{k_f(T_w - T_\infty)}$ denotes the Brinkman number.

Numerical solution procedure

Shooting method

Obtaining the exact analytical solutions from highly non-linear problems is considerably difficult. Thus, the shooting method is employed via `bvp4c` in MATLAB, which is a finite difference code that implements the three-stage Lobatto–IIIa formula, which is fourth-order accurate uniformly in the interval of integration. The mesh selection is based on the residual of the continuous solution. More details on the theoretical and practical backgrounds of `bvp4c` can be found in [55].

Before using the shooting method, higher-order ODEs must be converted into a set of first-order ODEs. Let

$$\begin{aligned} f &= y(1); & f' &= y(2); & f'' &= y(3); & f''' &= y(4) \\ f'''' &= yy1; & \theta &= y(5); & \theta' &= y(6); & \theta'' &= yy2. \end{aligned} \tag{23}$$

$$\begin{aligned} yy1 &= \frac{\varphi_1 \varphi_2 (1 + \lambda_2)}{\beta_3 y(1)} \left(-\beta_1 (y(1)^2 y(4) - 2y(1)y(2)y(3)) \right. \\ &+ \frac{1}{\varphi_1 \varphi_2 (1 + \lambda_2)} \left(\left(1 + \frac{1}{\beta}\right) y(4) + \beta_3 y(3)^2 \right) \\ &\left. - \frac{K}{\varphi_1 \varphi_2} y(2) - M \frac{\varphi_4}{\varphi_2} \sin^2(\Gamma) y(2) - y(2)^2 + y(1)y(3) \right) \end{aligned} \tag{24}$$

Table 4 Comparing the values of $-f''(0)$ with different values of S for $\varphi = \beta_1 = \lambda_2 = \beta_3 = K = M = \Lambda = 0$.

S	Ref. [57]	Ref. [58]	Ref. [49]	This study
0	0.677648	0.6776563	0.6776564	0.677653
0.5	0.873643	0.8736447	0.8736448	0.873644
0.75	0.984439	0.9844401	0.9844402	0.984440

Table 5 Comparing the values of $-\theta'(0)$ with different values of the Prandtl number for $\varphi = \beta_1 = \lambda_2 = \beta_3 = K = M = N_r = Q = Ec = N_t = \Lambda = S = Bi_T = 0$

Pr	Ref. [56]	Ref. [59]	Ref. [8]	Ref. [44]	This study
0.2	0.1691	0.1691	0.1691	0.1691	0.1690
0.7	0.4539	0.4539	0.4539	0.4537	0.4539
2	0.9114	0.9114	0.9114	0.9114	0.9114
7	1.8954	1.8954	1.8954	1.8954	1.8954

$$\begin{aligned} yy2 &= -\frac{1}{\varphi_5 \frac{1}{Pr} + N_r} \left(\varphi_3 y(1)y(6) + Qy(5) + \frac{Ec}{\varphi_1} y(3)^2 \right. \\ &\left. + N_t \varphi_3 y(6)^2 + \varphi_4 M Ec \sin^2(\Gamma) y(2)^2 \right) \end{aligned} \tag{25}$$

$$\begin{aligned} y0(2) &= 1 + \Lambda y0(3), & y0(1) &= S, \\ y0(6) &= -Bi_T(1 - y0(5)), & yinf(2) &\rightarrow 0, \\ yinf(5) &\rightarrow 0 \end{aligned} \tag{26}$$

Validation of the numerical code

To authenticate the current study, the current findings were tested against previous studies [8, 44, 49, 56–59]; the comparisons are listed in Tables 4 and 5. Overall, the agreement with previous studies provides confidence to proceed with the current study.

Results and discussion

The effects of the parameters controlling the flow on Casson–Maxwell, Casson–Jeffrey, and Casson–Oldroyd-B copper-engine oil binary nanofluids in a PTSC are presented in Figs. 3–27 and Tables 6, 7. The objectives of this study are to compare the three nanofluids and to determine the parameters that improve the efficiency of the device. The default parameter values are taken as follows: $\beta = 1; \beta_1 = \beta_3 = \lambda_2 = 0.5; K = 0.6; M = 0.2; \Gamma = \frac{\pi}{2}; S = 0.2, \Lambda = 0.3494; \varphi = 0.2; Pr = 7; N_r = Ec = 0.2; Q = 0.1; N_t = 0.15; Bi_T = 0.1; Re = B_K = 5; \text{ and } \Omega = 0.5; m = 3$

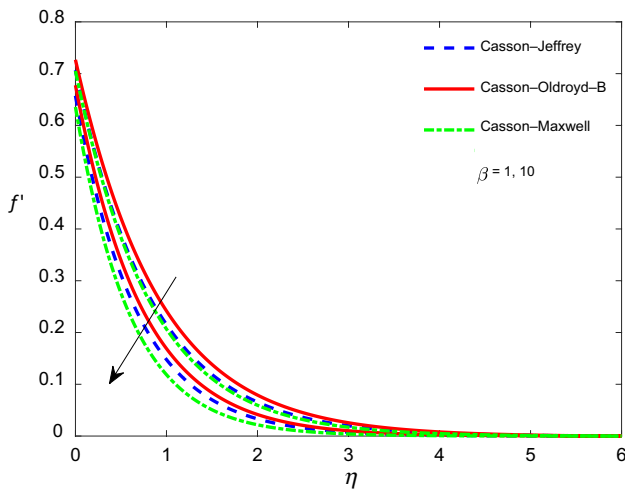


Fig. 3 The effect of β on f'

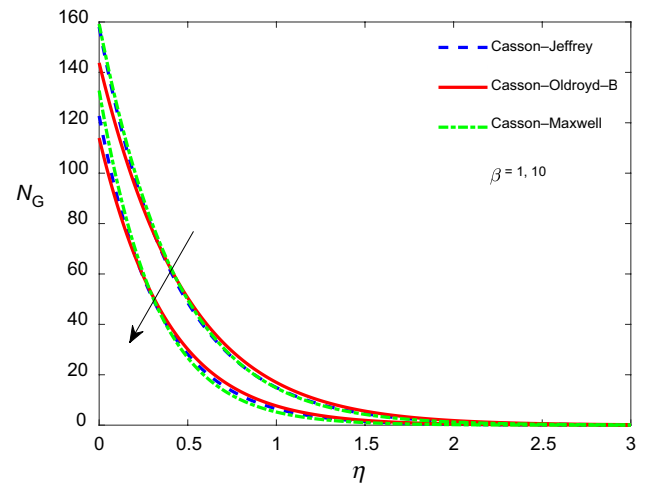


Fig. 5 The effect of β on N_G

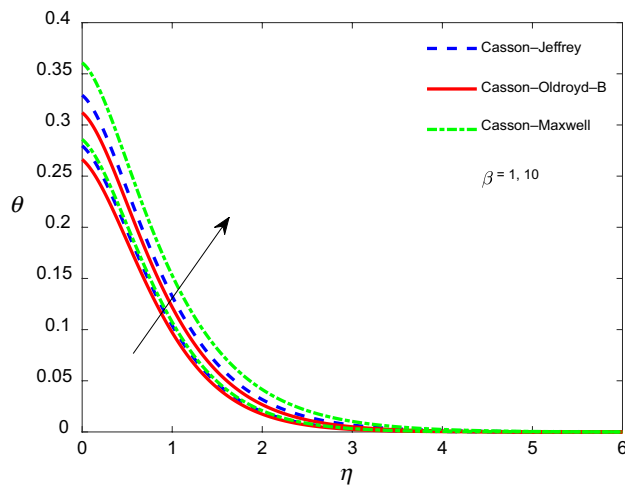


Fig. 4 The effect of β on θ

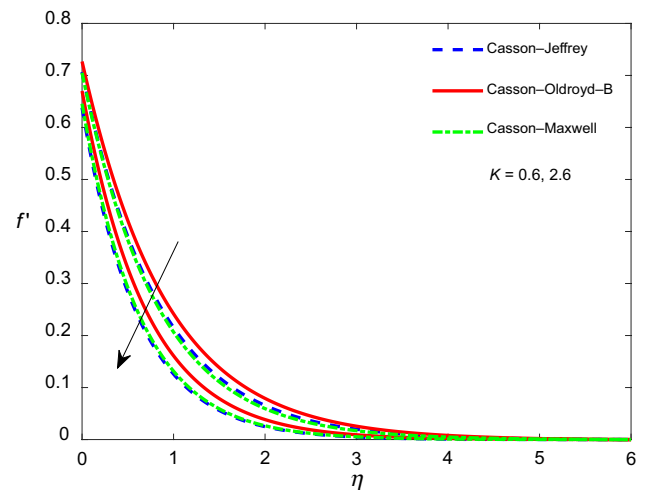


Fig. 6 The effect of K on f'

Effect of Casson parameter β

When the Casson parameter β is increased, the resistance to the flow also increases; consequently, a reduction in velocity is presented in Fig. 3. The Casson–Maxwell nanofluid exhibited the greatest resistance among the three binary nanofluids. The decrease in velocity extends the time allowed for the fluid to gain more heat, resulting in improved heat transferability. As presented in Fig. 4, the Casson–Maxwell nanofluid is the most enhanced in terms of heat transfer capabilities of the three binary nanofluids. Figure 5 shows that the entropy generation decreased with the increasing β as the increase in β reduces the rheological features, resulting in a faster shearing along the surface [60, 61]. At the

wall, the Casson–Maxwell nanofluid had the highest N_G , followed by the Casson–Jeffrey nanofluid, and then the Casson–Oldroyd–B nanofluid, whereas far from the wall, the Casson–Oldroyd–B nanofluid had the highest N_G , followed by the Casson–Jeffrey nanofluid, and then the Casson–Maxwell nanofluid.

Effect of the porosity parameter K

Large values of the porosity parameter contribute against the fluidity, resulting in a reduction in the velocity profile and an increase in both heating and irreversible energy (Figs. 6–8). Physically, the increase in the porosity parameter decreases nanoparticle collision owing to an increase in the size of the flow pore, inhibiting heat generation. The viscous force controls the buoyancy force, thereby

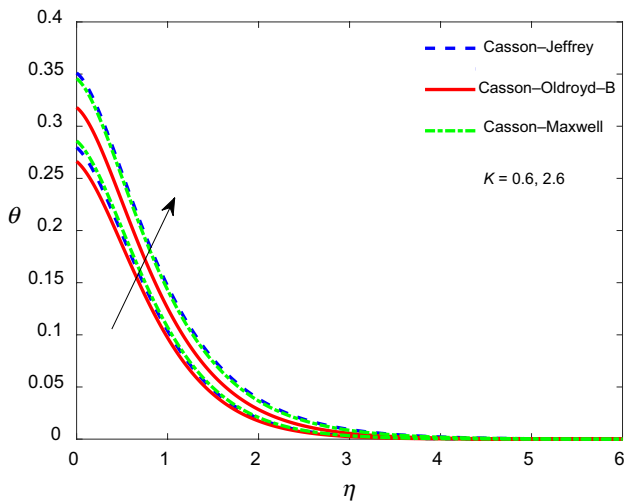


Fig. 7 The effect of K on θ

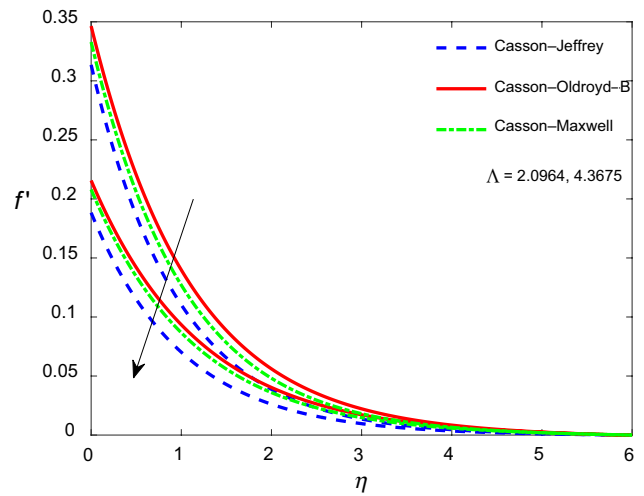


Fig. 9 The effect of Λ on f'

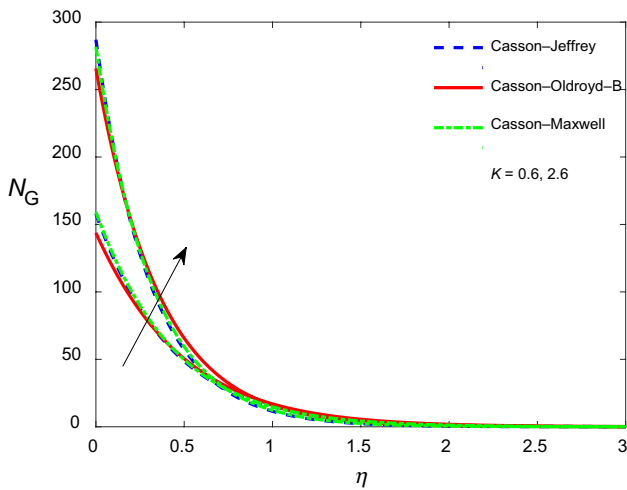


Fig. 8 The effect of K on N_G

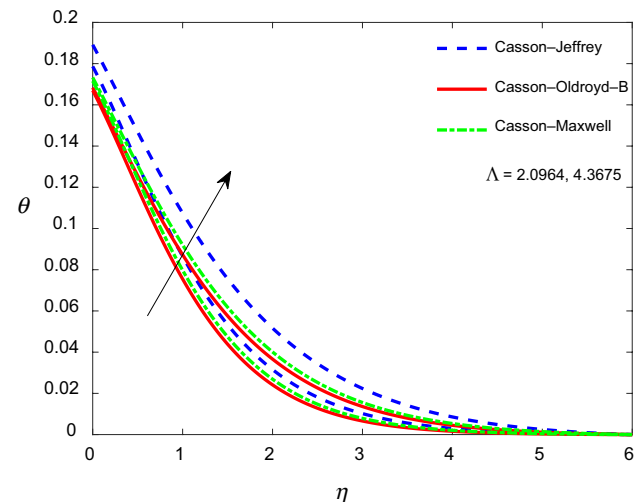


Fig. 10 The effect of Λ on θ

decreasing the flow magnitude. The entropy increased owing to existence of considerable temperature gradient at the surface [8, 38]. The most affected of the three nanofluids was the Casson–Jeffrey nanofluid, with the highest heat transfer and an entropy level close to that of the Casson–Maxwell nanofluid. The Casson–Oldroyd-B nanofluid exhibited the lowest heat transfer and highest entropy. The effect of K on the velocity, temperature, and entropy profiles is the same as that reported by previous studies [8, 38, 45].

Effect of the velocity slip parameter Λ

The friction force between the flow and the surface increases with increasing Λ , leading to an increase in viscosity and hence a decrease in velocity (Fig. 9). The decrease in velocity is accompanied by an increase in temperature owing to less heat being transported from one point to another (Fig. 10). Figure 11 clearly shows that the entropy decreases with increasing Λ . Generally, no-slip boundary conditions produce large velocity and temperature gradients, causing high entropy values. However, slip boundary conditions as in this study cause reduction in entropy close to the stretching

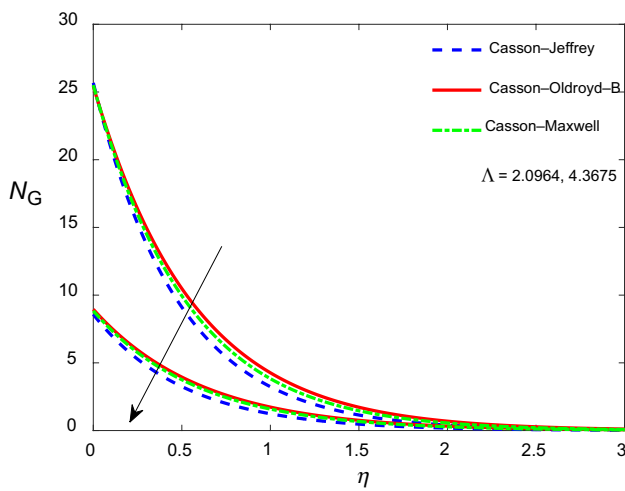


Fig. 11 The effect of Λ on N_G

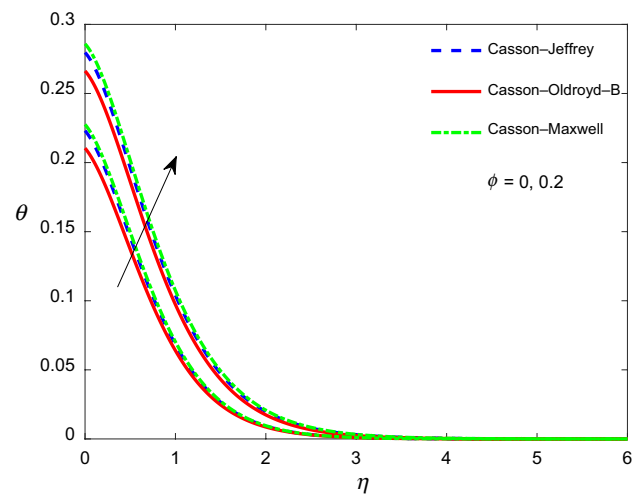


Fig. 13 The effect of φ on θ

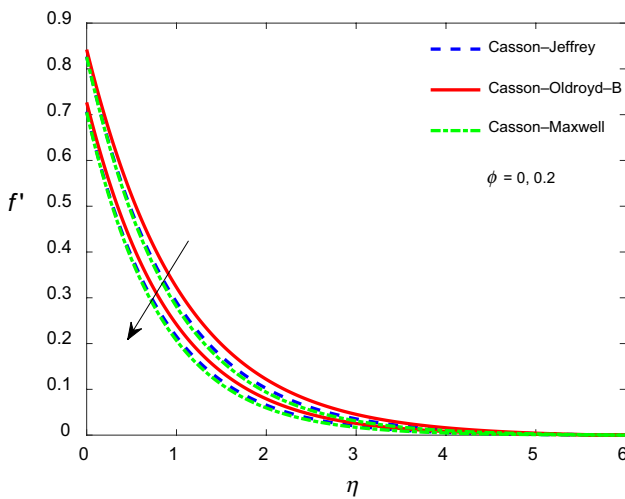


Fig. 12 The effect of φ on f'

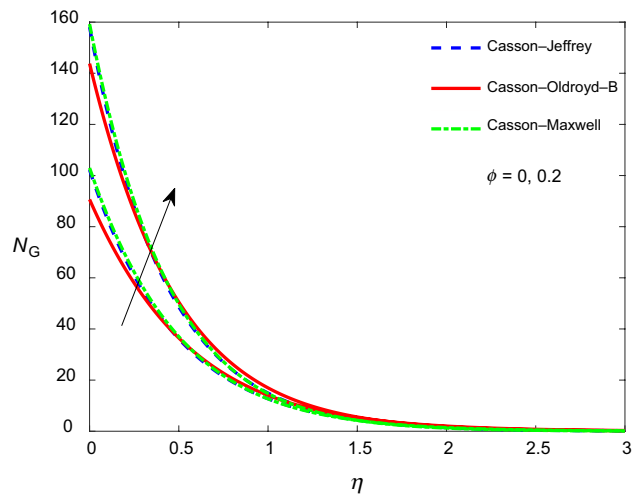


Fig. 14 The effect of φ on N_G

wall [7, 8]. Although the Casson–Jeffrey nanofluid exhibited a substantial heat profile enhancement, the Casson–Oldroyd-B nanofluid continued to exhibit low heat transfer and a high irreversible energy drain. The effect of Λ on the velocity, temperature, and entropy profiles is the same as that reported by previous studies [7, 8, 38, 45, 52].

Effect of the nanoparticle concentration parameter φ

The fluid viscosity increases with increasing φ owing to an increase in nanoparticle concentration and friction escalations, resulting in a decrease in velocity, as shown in Fig. 12. Because fluid velocity is critical for heat transfer,

the reduction in velocity causes heat to accumulate, and the temperature profile increases as observed in Fig. 13. It is expected that the entropy increases owing to heat accumulation [7, 8], which is confirmed in Fig. 14. Of the three nanofluids, Casson–Maxwell nanofluid benefited the most, as it underwent the highest improvement in terms of heat transfer. The effect of φ on the velocity, temperature, and entropy profiles is the same as that reported by previous studies [7, 8, 38, 45, 52].

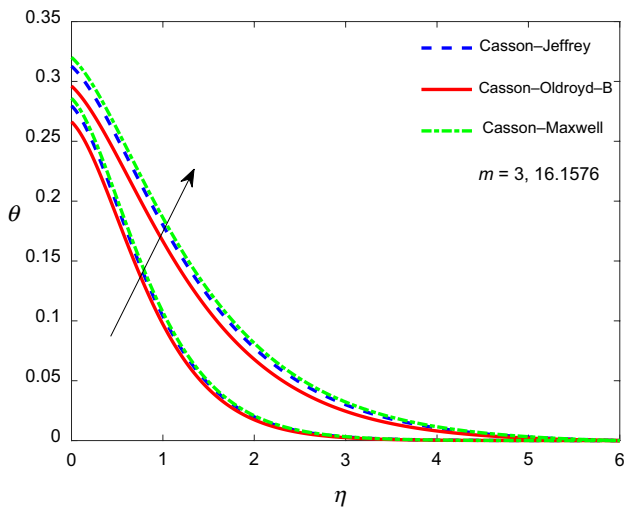


Fig. 15 The effect of m on θ

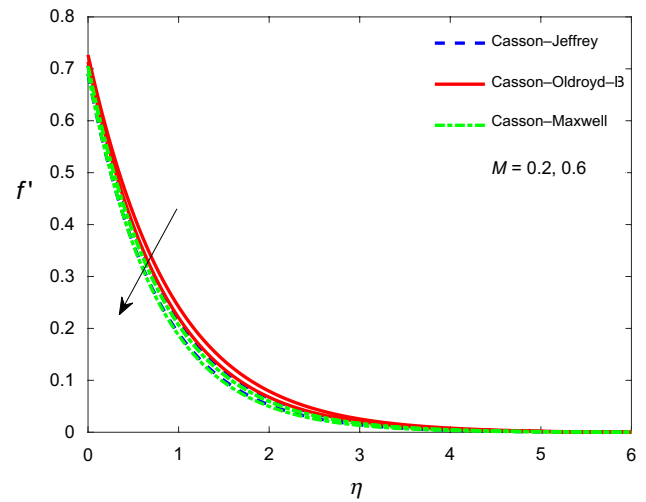


Fig. 17 The effect of M on f'

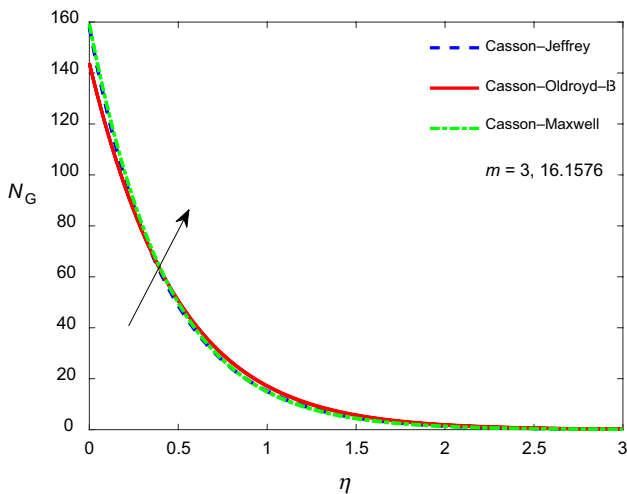


Fig. 16 The effect of m on N_G

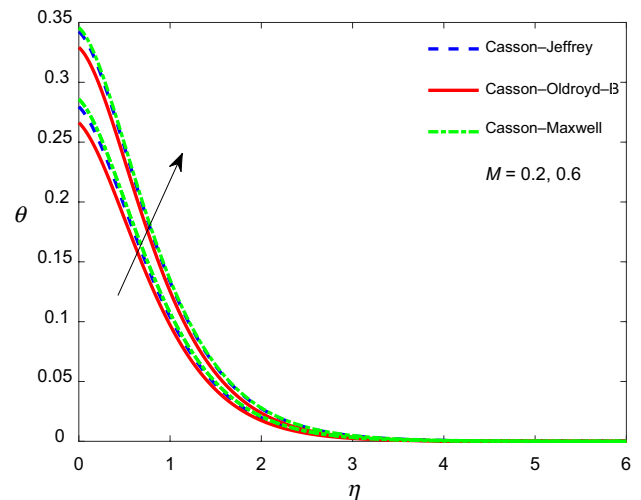


Fig. 18 The effect of M on θ

Effect of the nanoparticle shape factor m

Increasing shape factor values m by changing the nanoparticle shapes improves heat transferability. Figures 15 and 16 demonstrate that a lamina shape is the most effective in terms of heat transfer while causing a negligible increase in irreversible energy. Among the three nanofluids, the Casson–Maxwell nanofluid exhibited the highest heat transfer after increasing the shape factor. The effect of m on the temperature and entropy profiles is the same as that reported by a previous study [52].

Effect of the magnetic number M

Figure 17 shows the effect of M on the velocity profile. As the strength of the magnetic field increases, the drag force increases, which reduces the velocity of the nanofluid flow. Figure 18 confirms the fact that temperature distribution increases with increasing magnetic field because less heat can be transferred from one point to another with decreasing fluid movement. The lack of heat transfer in the system causes a natural increase in entropy [7], which is seen in Fig. 19. The Casson–Oldroyd-B nanofluid exhibited the lowest heat transfer. The effect of M on the velocity,

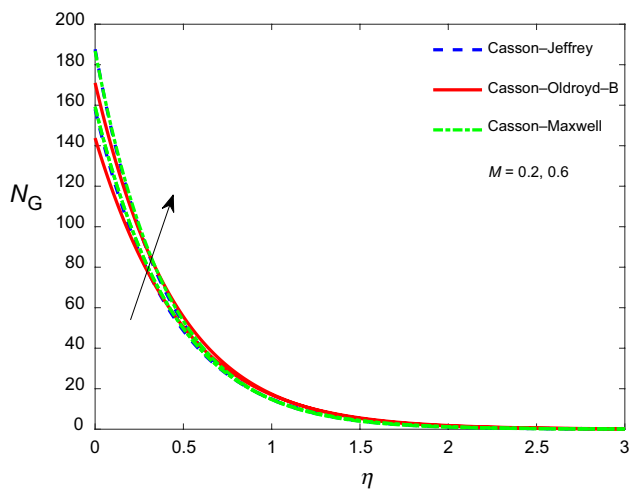


Fig. 19 The effect of M on N_G

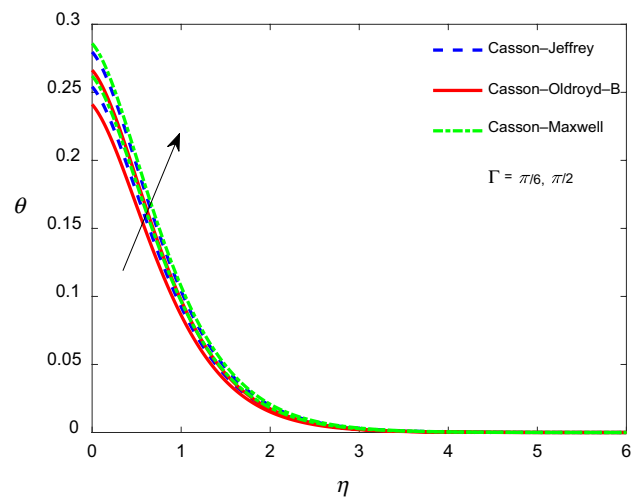


Fig. 21 The effect of Γ on θ

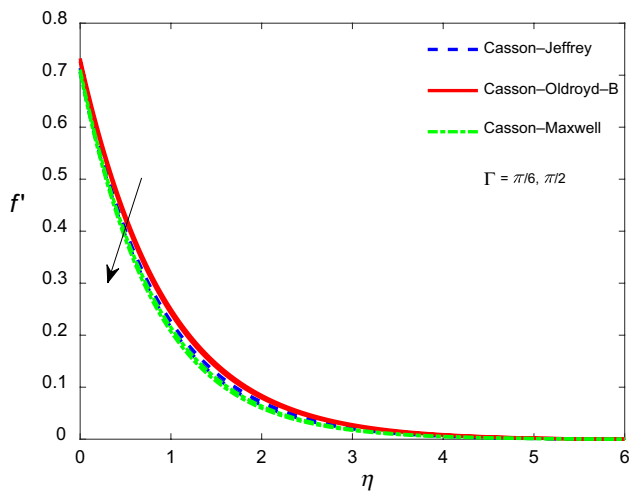


Fig. 20 The effect of Γ on f'

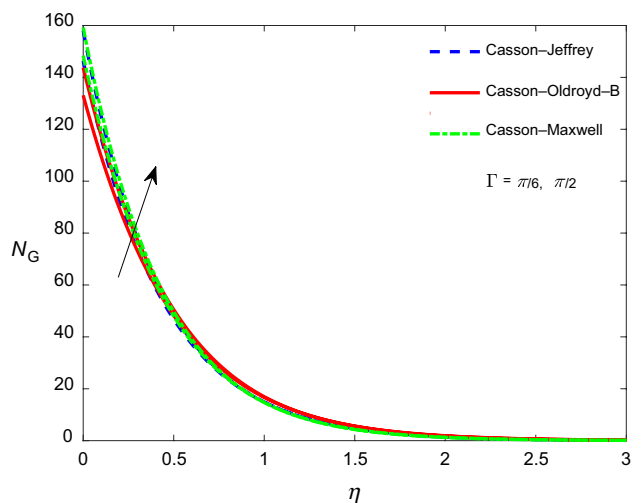


Fig. 22 The effect of Γ on N_G

temperature, and entropy profiles is the same as that reported by a previous study [7].

Effect of the magnetic angle of inclination Γ

As Γ increases from $\frac{\pi}{6}$ to $\frac{\pi}{2}$, the normal magnetic forces increase, resulting in a decrease in velocity. The reduced velocity will cause the temperature distribution to increase owing to low heat relocation from the surface toward the flow. The heat accumulation will intensify entropy generation in the system. Heat transferability and entropy are therefore increased, with the Casson–Maxwell

nanofluid exhibiting the highest heat transferability as seen in Figs. 20–22. The effect of Γ on the velocity, temperature, and entropy profiles is the same as that reported by a previous study [7].

Effect of the thermal Biot number Bi_T

The thermal Biot number describes the ratio between thermal resistances inside the fluid and at the surface. Hence, large values of Bi_T amplify the thermal resistance inside the flow, which increases the fluid temperature. The

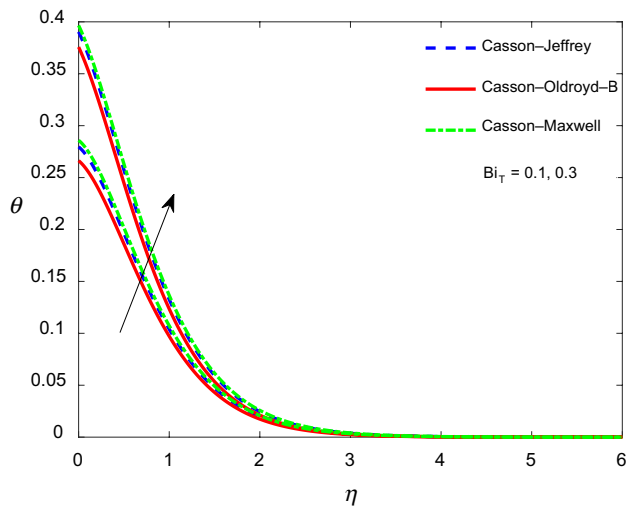


Fig. 23 The effect of Bi_T on θ

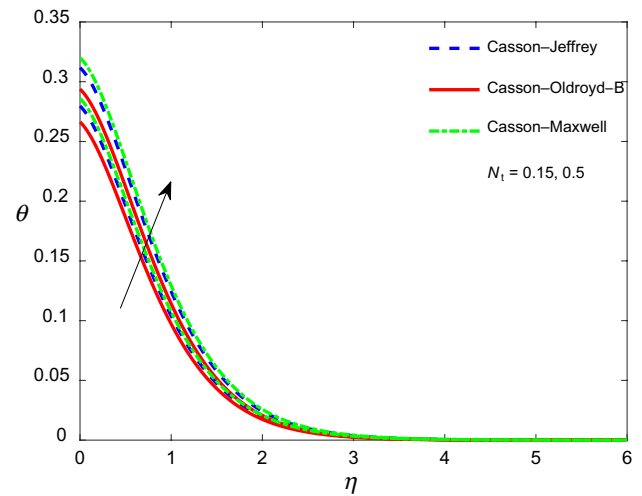


Fig. 25 The effect of N_t on θ

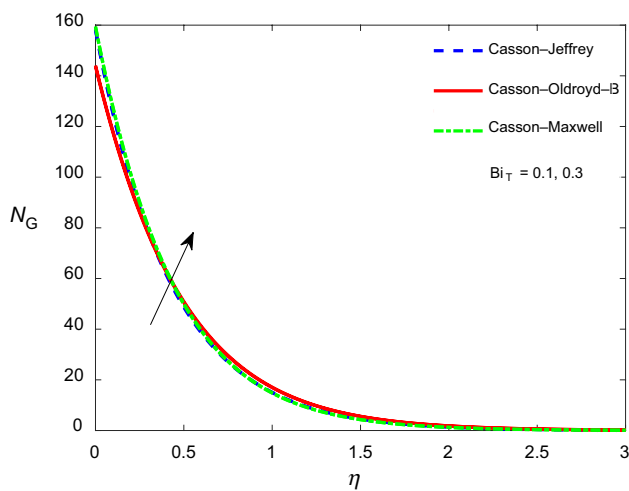


Fig. 24 The effect of Bi_T on N_G

increase in Bi_T values leads to an increase in the heat transfer rate and the entropy generated by the system [7], which is illustrated in Figs. 23 and 24. Of the three nanofluids, the Casson–Oldroyd–B nanofluid exhibits the lowest heat transfer. The effect of Bi_T on the temperature and entropy profiles is the same as that reported by previous studies [7, 45].

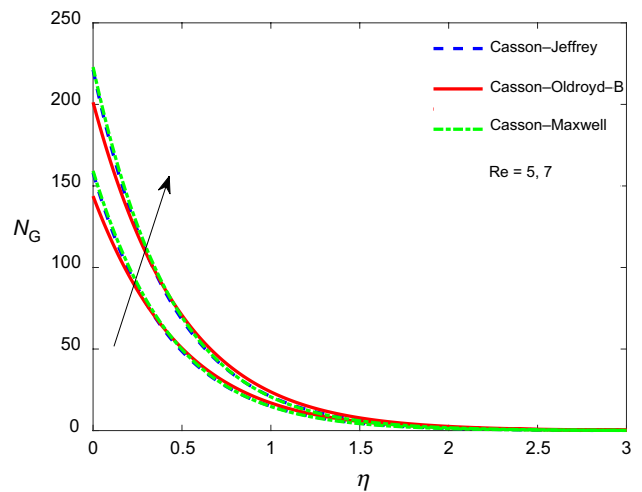


Fig. 26 The effect of Re on N_G

Effect of thermophoretic parameter N_t

Higher values of the thermophoretic parameter indicate larger thermophoretic force, which appears in suspended mixtures of particles and fluids such as nanofluids. This phenomenon is caused by the temperature gradient which

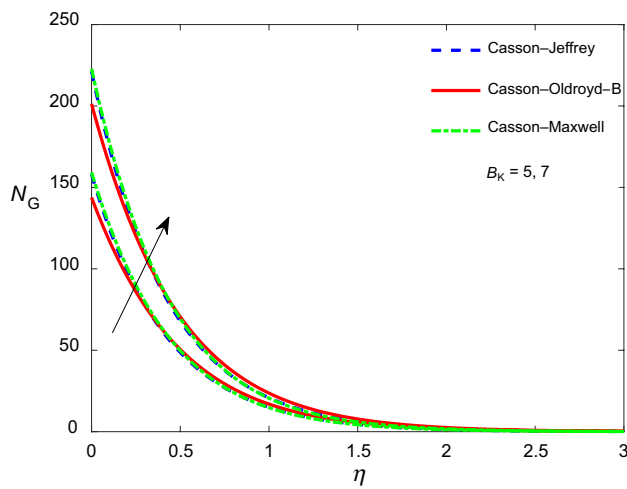


Fig. 27 The effect of B_K on N_G

leads to a movement of fluid particles in the hot zone toward the cold region. Hence, heat transfer capabilities increase as seen in Fig. 25. The highest heat transfer was

observed in the Casson–Maxwell and Casson–Jeffrey nanofluids.

Effects of the Reynolds number Re and the Brinkman number B_K

At high values of Re , the resistive forces replace the viscous forces. Further, the Brinkman number measures the dominant effects responsible for variation in irreversible energy drain. It determines whether heat is transferred or dissipated through conduction at the surface. The increase in B_K values as in this case, causes an increase in entropy generation which indicates the dominant effect of dissipation [7]. Notably, increasing Re or B_K increases the irreversible energy drain, as seen in Figs. 26 and 27. The difference among the three nanofluids was found to be marginal. The effects of Re and B_K on the velocity, temperature, and entropy profiles are the same as that reported by previous studies [7, 8, 38, 45].

Table 6 Computing skin friction constant C_f values

β	φ	K	M	Γ	S	Λ	$C_f Re_x^{-\frac{1}{2}}$ (Casson–Maxwell)	$C_f Re_x^{-\frac{1}{2}}$ (Casson–Jeffrey)	$C_f Re_x^{-\frac{1}{2}}$ (Casson–Oldroyd-B)
1	0.2	0.6	0.2	$\frac{\pi}{2}$	0.2	0.3494	-2.9486	-1.9555	-2.7323
5							-2.1219	-1.3432	-1.8925
10							-2.0041	-1.2568	-1.7734
	0.1						-2.1438	-1.4260	-1.9855
	0.15						-2.5188	-1.6716	-2.3337
	0.2						-2.9486	-1.9555	-2.7323
		0.6					-2.9486	-1.9555	-2.7323
		1.6					-3.2786	-2.2129	-3.0457
		2.6					-3.5437	-2.4120	-3.2988
			0.2				-2.9486	-1.9555	-2.7323
			0.4				-3.0215	-2.0134	-2.8013
			0.6				-3.0906	-2.0678	-2.8669
				$\frac{\pi}{12}$			-2.8770	-1.8979	-2.6646
				$\frac{\pi}{6}$			-2.8913	-1.9095	-2.6781
				$\frac{\pi}{2}$			-2.9486	-1.9555	-2.7323
					0.1		-2.8115	-1.9141	-2.6317
					0.2		-2.9486	-1.9555	-2.7323
					0.3		-3.0986	-1.9955	-2.8364
						0.1747	-3.6274	-2.3471	-3.2786
						0.3494	-2.9486	-1.9555	-2.7323
						0.5241	-2.5014	-1.6811	-2.3535

Table 7 Computing local Nusselt number Nu_x values

β	φ	K	M	Λ	Pr	N_r	Q	N_t	Ec	Bi_T	m	$Nu_x Re_x^{-\frac{1}{2}}$ (Casson–Maxwell)	$Nu_x Re_x^{-\frac{1}{2}}$ (Casson–Jeffrey)	$Nu_x Re_x^{-\frac{1}{2}}$ (Casson–Oldroyd-B)
1	0.2	0.6	0.2	0.3494	7	0.2	0.1	0.15	0.2	0.1	3	0.1499	0.1512	0.1539
5												0.1370	0.1425	0.1459
10												0.1343	0.1409	0.1444
	0.1											0.1209	0.1216	0.1234
	0.18											0.1438	0.1450	0.1475
	0.2											0.1499	0.1512	0.1539
		0.6										0.1499	0.1512	0.1539
		1.6										0.1434	0.1433	0.1483
		2.6										0.1374	0.1364	0.1432
			0.2									0.1499	0.1512	0.1539
			0.6									0.1373	0.1380	0.1408
			0.8									0.1315	0.1320	0.1346
				0.1747								0.1370	0.1407	0.1440
				0.3494								0.1499	0.1512	0.1539
				0.6988								0.1623	0.1622	0.1644
					6							0.1494	0.1507	0.1535
					7							0.1499	0.1512	0.1539
					9							0.1504	0.1517	0.1544
						0.1						0.1381	0.1393	0.1418
						0.2						0.1499	0.1512	0.1539
						0.3						0.1610	0.1625	0.1656
							0.1					0.1499	0.1512	0.1539
							0.2					0.1382	0.1401	0.1443
							0.3					0.1167	0.1203	0.1285
								0.1				0.1507	0.1520	0.1546
								0.15				0.1499	0.1512	0.1539
								0.2				0.1490	0.1503	0.1532
									0.1			0.1714	0.1721	0.1737
									0.2			0.1499	0.1512	0.1539
									0.5			0.0811	0.0845	0.0914
										0.1		0.1499	0.1512	0.1539
										0.2		0.2748	0.2774	0.2833
										0.4		0.3800	0.3838	0.3930
											3	0.1499	0.1512	0.1539
											6.3698	0.2195	0.2215	0.2259
											16.1576	0.4114	0.4155	0.4247

Conclusions

The copper-engine oil Casson–Maxwell, Casson–Jeffrey, and Casson–Oldroyd-B binary nanofluids were compared in PTSC settings. Porosity, constant inclined magnetic field, heat source, thermal radiation, viscosity dissipation, and thermophoresis were considered. Analysis was conducted by formulating the continuity, momentum, and energy equations. Subsequently, similarity variables were used to transform the partial differential equations into ODEs, which were then solved using the shooting method.

There are various practical applications for the presented models, including solar water pumps, solar-powered ships, solar street lights, solar energy plates, and photovoltaic cells. Overall, an increase in PTSC efficiency can be achieved by decreasing the nanofluid velocity and boosting the nanofluid temperature while maintaining reasonable entropy generation. The key conclusions of this numerical study are as follows:

- The parameters that reduced the velocity profile are β , K , Λ , φ , M , and Γ .
- The parameters that enhanced heat transfer are β , K , Λ , φ , m , M , Γ , Bi_T , and N_t .
- Entropy generation increased with K , φ , m , M , Γ , Bi_T , Re , and B_K but decreased with β and Λ .
- The skin friction values increased with φ , K , M , Γ , and S but decreased with β and Λ .
- The local Nusselt number values increased with φ , Λ , Pr , N_t , Bi_T , and m but decreased with β , K , M , Q , N_t , and E_c .
- The Casson–Oldroyd-B nanofluid consistently exhibited the lowest heat transfer and highest generated entropy.
- The Casson–Jeffrey and Casson–Maxwell nanofluids responded differently to the change in parameters. Casson–Maxwell had better heat transfer with β , φ , m , M , Γ , N_t , and Bi_T , whereas Casson–Jeffrey had better heat transfer with K and Λ .
- From the aforementioned discussion, we conclude that the Casson–Maxwell and Casson–Jeffrey nanofluids exhibit similar performance in a PTSC setting, with a slight preference to use the Casson–Maxwell nanofluid.

Limitations and further research

This study is limited to the three binary nanofluids and PTSC settings mentioned herein. As any different nanofluid will have different properties and can lead to different results. Further, different settings will require different assumptions and boundary conditions, which will also lead to different results.

Further research can be directed toward theoretical investigation of different nanofluid models (e.g., Carreau, Walter-B, etc.) in PTSC settings and their comparison. Additionally, the presented model can be generalized by considering the impact of time-dependent flow and temperature-dependent viscosity, conductivity, and porosity on the performance of PTSCs. It is also important to explore the effect of hybrid nanoparticles on the PTSC performance using different binary nanofluid models.

Acknowledgements The authors would like to express their gratitude to the reviewers for their constructive comments that have significantly contributed to the enrichment of this study.

Author contributions PBR helped in data curation, software, formal analysis, writing manuscript. FNI contributed to formal analysis, validation, project administration. All authors have approved the final article.

Funding Open access funding provided by The Science, Technology & Innovation Funding Authority (STDF) in cooperation with The Egyptian Knowledge Bank (EKB). The authors declare that no funds, grants, or other supports were received during the preparation of this manuscript.

Data availability Correspondence and requests for materials should be addressed to F.N.I.

Declaration

Competing interest The authors declare that they have no known competing financial interests or personal relationships that could have appeared to influence the work reported in this paper.

Open Access This article is licensed under a Creative Commons Attribution 4.0 International License, which permits use, sharing, adaptation, distribution and reproduction in any medium or format, as long as you give appropriate credit to the original author(s) and the source, provide a link to the Creative Commons licence, and indicate if changes were made. The images or other third party material in this article are included in the article's Creative Commons licence, unless indicated otherwise in a credit line to the material. If material is not included in the article's Creative Commons licence and your intended use is not permitted by statutory regulation or exceeds the permitted use, you will need to obtain permission directly from the copyright holder. To view a copy of this licence, visit <http://creativecommons.org/licenses/by/4.0/>.

References

1. Kalogirou SA. Solar thermal collectors and applications. *Prog Energy Combust Sci.* 2004;30:231–95. <https://doi.org/10.1016/j.pecs.2004.02.001>.
2. Choi S. Enhancing thermal conductivity of fluids with nanoparticles. *IMECE.* 1995;66:99–105.
3. Ekiciler R, Arslan K, Turgut O, Kursun B. Effect of hybrid nanofluid on heat transfer performance of parabolic trough solar collector receiver. *J Therm Anal Calorim.* 2021;143:1637–54. <https://doi.org/10.1007/s10973-020-09717-5>.
4. Bellos E, Tzivanidis C, Said Z. A systematic parametric thermal analysis of nanofluid-based parabolic trough solar collectors. *Sustain Energy Technol Assess.* 2020. <https://doi.org/10.1016/j.seta.2020.100714>.
5. Razmmand F, Mehdipour R, Mousavi SM. A numerical investigation of nanofluids on heat transfer of the solar parabolic trough collectors. *Appl Therm Eng.* 2019;152:624–33. <https://doi.org/10.1016/j.applthermaleng.2019.02.118>.
6. Ajbar W, Parrales A, Huicochea A, Hernandez JA. Different ways to improve parabolic trough solar collectors' performance over the last four decades and their applications: a comprehensive review. *Renew Sustain Energy Rep.* 2022. <https://doi.org/10.1016/j.rser.2021.111947>.
7. Shahzad F, Jamshed W, Safdar R, Hussain SM, Nasir NAAM, Dhange M, Nisar KS, Eid MR, Sohail M, Alsehli M, Elfaskhany A. Thermal analysis characterization of solar-powered ship using Oldroyd hybrid nanofluids in parabolic trough solar collector: an optimal thermal application. *Nanotechnol Rev.* 2022;11:2015–37. <https://doi.org/10.1515/ntrev-2022-0108>.
8. Jamshed W, Sirin C, Selimefendigil F, Shamshuddin MD, Altowairqi Y, Eid MR. Thermal characterization of coolant Maxwell type nanofluid flowing in parabolic trough solar collector (PTSC) used inside solar powered ship application. *Coatings.* 2021;12:1552. <https://doi.org/10.3390/coatings11121552>.
9. Jamshed W, Shahzad F, Safdar R, Sajid T, Eid MR, Nisar KS. Implementing renewable solar energy in presence of Maxwell nanofluid in parabolic trough solar collector: a computational study. *Waves Random Complex Media.* 2021. <https://doi.org/10.1080/17455030.2021.1989518>.
10. Nabwey HA, Reddy MG, Kumar BKN, Sandeep N. Effect of resistive and radiative heats on enhanced heat transfer of parabolic

- trough solar collector. *J Process Mech Eng.* 2022. <https://doi.org/10.1177/09544089221117317>.
11. Kumar S, Ghosh S, Samet B, Goufo EFD. An analysis for heat equations arises in diffusion process using new Yang–Abdel–Aty–Cattani fractional operator. *Math Methods Appl Sci.* 2020;43:6062–80. <https://doi.org/10.1002/mma.6347>.
 12. Kumar S, Kumar A, Baleanu D. Two analytical methods for time-fractional nonlinear coupled Boussinesq–Burger’s equations arise in propagation of shallow water waves. *Nonlinear Dyn.* 2016;85:699–715. <https://doi.org/10.1007/s11071-016-2716-2>.
 13. Kumar S, Nisar KS, Kumar R, Cattani C, Samet B. A new Rabotnov fractional-exponential function based fractional derivative for diffusion equation under external force. *Math Methods Appl Sci.* 2020;43:4460–71. <https://doi.org/10.1002/mma.6208>.
 14. Veerasha P, Prakasha DG, Kumar S. A fractional model for propagation of classical optical solitons by using nonsingular derivative. *Math Methods Appl Sci.* 2020. <https://doi.org/10.1002/mma.6335>.
 15. Alshabanat A, Jleli M, Kumar S, Samet B. Generalization of the Caputo–Fabrizio fractional derivative and applications to electrical circuits. *Front Phys.* 2020;8:1–10. <https://doi.org/10.3389/fphy.2020.00064>.
 16. Shafqat H, Zehba R, Abdelraheem MA. Thermal radiation impact on bioconvection flow of nano-enhanced phase change materials and oxytactic microorganisms inside a vertical wavy porous cavity. *Int Commun Heat Mass Transf.* 2022. <https://doi.org/10.1016/j.icheatmasstransfer.2022.106454>.
 17. Shafqat H, Abdelraheem MA, Noura A. Bioconvection of oxytactic microorganisms with nano-encapsulated phase change materials in an omega-shaped porous enclosure. *J Energy Storage.* 2022. <https://doi.org/10.1016/j.est.2022.105872>.
 18. Shafqat H, Noura A, Abdelraheem MA. Natural convection of a water-based suspension containing nano-encapsulated phase change material in a porous grooved cavity. *J Energy Storage.* 2022. <https://doi.org/10.1016/j.est.2022.104589>.
 19. Shafqat H, Abdelraheem MA, Hakan FÖ. Magneto-bioconvection flow of hybrid nanofluid in the presence of oxytactic bacteria in a lid-driven cavity with a streamlined obstacle. *Int Commun Heat Mass Transf.* 2022. <https://doi.org/10.1016/j.icheatmasstransfer.2022.106029>.
 20. Shafqat H, Muhammad J, Zoubida H, Arıcı M. Numerical modeling of magnetohydrodynamic thermosolutal free convection of power law fluids in a staggered porous enclosure. *Sustain Energy Technol Assess.* 2022. <https://doi.org/10.1016/j.seta.2022.102395>.
 21. Kumar KG, Ramesh GK, Gireesha BJ, Gorla RSR. Characteristics of Joule heating and viscous dissipation on three-dimensional flow of Oldroyd B nanofluid with thermal radiation. *Alex Eng J.* 2018;57:2139–49. <https://doi.org/10.1016/j.aej.2017.06.006>.
 22. Gireesha BJ, Kumar KG, Ramesh GK, Prasannakumara BC. Non-linear convective heat and mass transfer of Oldroyd-B nanofluid over a stretching sheet in the presence of uniform heat source/sink. *Results Phys.* 2018;9:1555–63. <https://doi.org/10.1016/j.rinp.2018.04.006>.
 23. Kumar KG, Gireesha BJ, Krishnamurthy MR, Rudraswamy NG. An unsteady squeezed flow of a tangent hyperbolic fluid over a sensor surface in the presence of variable thermal conductivity. *Results Phys.* 2017;7:3031–6. <https://doi.org/10.1016/j.rinp.2017.08.021>.
 24. Reddy MG, Rani MVVLS, Kumar KG, Prasannakumara BC. Cattaneo–Christov heat flux and non-uniform heat-source/sink impacts on radiative Oldroyd-B two-phase flow across a cone/wedge. *J Braz Soc Mech Sci Eng.* 2018. <https://doi.org/10.1007/s40430-018-1033-8>.
 25. Sureshkumar RS, Kumar KG, Rahimi-Gorji M, Khan I. Darcy–Forchheimer flow and heat transfer augmentation of a viscoelastic fluid over an incessant moving needle in the presence of viscous dissipation. *Microsyst Technol.* 2019;25:3399–405. <https://doi.org/10.1007/s00542-019-04340-3>.
 26. Ramesh GK, Kumar KG, Shehzad SA, Gireesha BJ. Enhancement of radiation on hydromagnetic Casson fluid flow towards a stretched cylinder with suspension of liquid-particles. *Can J Phys.* 2017;96:18–24. <https://doi.org/10.1139/cjp-2017-0307>.
 27. Kumar KG, Rudraswamy NG, Gireesha BJ, Krishnamurthy MR. Influence of nonlinear thermal radiation and viscous dissipation on three-dimensional flow of Jeffrey nano fluid over a stretching sheet in the presence of Joule heating. *Nonlinear Eng.* 2017;6:207–19. <https://doi.org/10.1515/nleng-2017-0014>.
 28. Rudraswamy NG, Kumar KG, Gireesha BJ, Gorla RSR. Combined effect of joule heating and viscous dissipation on MHD three dimensional flow of a Jeffrey nanofluid. *J Nanofluids.* 2017;6:300–10. <https://doi.org/10.1166/jon.2017.1329>.
 29. Nourafkan E, Asachi M, Jin H, Wen D, Ahmed W. Stability and photo-thermal conversion performance of binary nanofluids for solar absorption refrigeration systems. *Renew Energy.* 2019;140:264–73. <https://doi.org/10.1016/j.renene.2019.01.081>.
 30. Zeng J, Xuan Y. Enhanced solar thermal conversion and thermal conduction of MWCNT-SiO₂/Ag binary nanofluids. *Appl Energy.* 2018;212:809–19. <https://doi.org/10.1016/j.apenergy.2017.12.083>.
 31. Ma M, Xie M, Ai Q. Study on photothermal properties of Zn-ZnO/paraffin binary nanofluids as a filler for double glazing unit. *Int J Heat Mass Transf.* 2022. <https://doi.org/10.1016/j.ijheatmasstransfer.2021.122173>.
 32. Nejad AS, Barzoki MF, Rahmani M, Kasaeian A, Hajinezhad A. Simulation of the heat transfer performance of Al₂O₃-Cu/water binary nanofluid in a homogenous copper metal foam. *J Therm Anal Calorim.* 2022;147:12495–512. <https://doi.org/10.1007/s10973-022-11487-1>.
 33. Yu Q. A decoupled wavelet approach for multiple physical flow fields of binary nanofluids in double-diffusive convection. *Appl Math Comput.* 2021. <https://doi.org/10.1016/j.amc.2021.126232>.
 34. Lee M, Shin Y, Cho H. Theoretical study on performance comparison of various solar collectors using binary nanofluids. *J Mech Sci Technol.* 2021;35:1267–78. <https://doi.org/10.1007/s12206-021-0238-4>.
 35. Reddy KV, Reddy GVR, Chamka AJ. Effects of viscous dissipation and thermal radiation on an electrically conducting Casson-Carreau nanofluids flow with Cattaneo–Christov heat flux model. *J Nanofluids.* 2022;11:214–26. <https://doi.org/10.1166/jon.2022.1836>.
 36. Oyelakin IS, Lalramneihmawai PC, Mondal S, Sibanda P. Analysis of double-diffusion convection on three dimensional MHD stagnation point flow of a tangent hyperbolic Casson nanofluid. *Int J Ambient Energy.* 2022;43:1854–65. <https://doi.org/10.1080/01430750.2020.1722964>.
 37. Yousef NS, Megahed AM, Ghoneim NI, Elsafi M, Fares E. Chemical reaction impact on MHD dissipative Casson-Williamson nanofluid flow over a slippery stretching sheet through porous medium. *Alex Eng J.* 2022;61:10161–70. <https://doi.org/10.1016/j.aej.2022.03.032>.
 38. Jamshed W, Nisar KS. Computational single-phase comparative study on a Williamson nanofluid in a parabolic trough solar collector via the Keller box method. *Int J Energy Rep.* 2021;45:10696–718. <https://doi.org/10.1002/er.6554>.
 39. Sharafeldin MA, Grof G, Abu-Nada E, Mahian O. Evacuated tube solar collector performance using copper nanofluid: energy and environmental analysis. *Appl Therm Eng.* 2019. <https://doi.org/10.1016/j.applthermaleng.2019.114205>.
 40. Dogonchi AS, Sheremet MA, Ganji DD, Pop I. Free convection of copper-water nanofluid in a porous gap between hot rectangular cylinder and cold circular cylinder under the effect of inclined

- magnetic field. *J Therm Anal Calorim.* 2019;135:1171–84. <https://doi.org/10.1007/s10973-018-7396-3>.
41. Olia H, Torabi M, Bahiraei M, Ahmadi MH, Goodarzi M, Safaei MR. Application of nanofluids in thermal performance enhancement of parabolic trough solar collector: state of the art. *Appl Sci.* 2019. <https://doi.org/10.3390/app9030463>.
 42. Lin Y, Li BT, Zheng L, Chen G. Particle shape and radiation effects on Marangoni boundary layer flow and heat transfer of copper-water nanofluid driven by an exponential temperature. *Powder Technol.* 2016;301:379–86. <https://doi.org/10.1016/j.powtec.2016.06.029>.
 43. Ellahi R, Zeeshan A, Hassan M. Particle shape effects on marangoni convection boundary layer flow of a nanofluid. *Int J Numer Methods Heat Fluid Flow.* 2016;26:2160–74. <https://doi.org/10.1108/HFF-11-2014-0348>.
 44. Alkathiri AA, Jamshed W, Devi SSU, Eid MR, Bouazizi ML. Galerkin finite element inspection of thermal distribution of renewable solar energy in presence of binary nanofluid in parabolic trough solar collector. *Alex Eng J.* 2022;61:11063–76. <https://doi.org/10.1016/j.aej.2022.04.036>.
 45. Ouni M, Ladhar L, Omri M, Jamshed W, Eid MR. Solar water-pump thermal analysis utilizing copper-gold/engine oil hybrid nanofluid flowing in parabolic trough solar collector: thermal case study. *Case Stud Therm Eng.* 2022;30:101756. <https://doi.org/10.1016/j.csite.2022.101756>.
 46. Hussain SM, Jamshed W. A comparative entropy based analysis of tangent hyperbolic hybrid nanofluid flow: implementing finite difference method. *Int Commun Heat Mass Transf.* 2021;129:105671. <https://doi.org/10.1016/j.icheatmasstransfer.2021.105671>.
 47. Pramanik S. Casson fluid flow past an exponentially porous stretching surface in presence of thermal radiation. *Ain Shams Eng J.* 2014;5:205–12. <https://doi.org/10.1016/j.asej.2013.05.003>.
 48. Sochi T. Flow of non-Newtonian fluids in porous media. *J Polym Sci B Polym Phys.* 2010;48:2437–767. <https://doi.org/10.1002/polb.22144>.
 49. Sandeep N, Sulochana C. Momentum and heat transfer behaviour of Jeffrey, Maxwell and Oldroyd-B nanofluids past a stretching surface with non-uniform heat source/sink. *Ain Shams Eng J.* 2018;9:517–24. <https://doi.org/10.1016/j.asej.2016.02.008>.
 50. Lim YJ, Shafie S, Isa SM, Rawi NA, Mohamad AQ. Impact of chemical reaction, thermal radiation and porosity on free convection Carreau fluid flow towards a stretching cylinder. *Alex Eng J.* 2022;61:4701–17. <https://doi.org/10.1016/j.aej.2021.10.023>.
 51. Reddy NB, Poornima T, Sreenivasulu P. Influence of variable thermal conductivity on MHD boundary layer slip flow of ethylene-glycol based Cu nanofluids over a stretching sheet with convective boundary convection. *Int J Eng Math.* 2014. <https://doi.org/10.1155/2014/905158>.
 52. Jamshed W, Devi SSU, Safdar R, Redouane F, Nisar KS, Eid MR. Comprehensive analysis on copper-ion (II, III)/oxide-engine oil Casson nanofluid flowing and thermal features in parabolic trough solar collector. *J Taibah Univ Sci.* 2021;15:619–36. <https://doi.org/10.1080/16583655.2021.1996114>.
 53. Xu X, Chen S. Cattaneo-Christov heat flux model for heat transfer of Marangoni boundary layer flow in a copper-water nanofluid. *Heat Trans Asian Res.* 2017;46:1281–93. <https://doi.org/10.1002/htj.21273>.
 54. Reddy M, Makinde OD. Magnetohydrodynamic peristaltic transport of Jeffrey nanofluid in an asymmetric channel. *J Mol Liq.* 2016;223:1242–8. <https://doi.org/10.1016/j.molliq.2016.09.080>.
 55. Keskin AÜ. Solution of BVPs Using bvp4c and bvp5c of MATLAB. In: *Boundary value problems for engineers.* Springer, Cham; 2019. p. 417–505. https://doi.org/10.1007/978-3-030-21080-9_10.
 56. Wang CY. Free convection on a vertical stretching surface. *J Appl Math Mech.* 1989;69:418–20. <https://doi.org/10.1002/zamm.19890691115>.
 57. Ferdows M, Uddin MJ, Afify AA. Scaling group transformation for MHD boundary layer free convective heat and mass transfer flow past a convectively heated nonlinear radiating stretching sheet. *Int J Heat Mass Transf.* 2013;56:181–7. <https://doi.org/10.1016/j.ijheatmasstransfer.2012.09.020>.
 58. Rashidi MM, Rostami B, Freidoonimehr N, Abbasbandy S. Free convective heat and mass transfer for MHD fluid flow over a permeable vertical stretching sheet in the presence of the radiation and buoyancy effects. *Ain Shams Eng J.* 2014;4:901–12. <https://doi.org/10.1016/j.asej.2014.02.007>.
 59. Gorla RSR, Sidawi I. Free convection on a vertical stretching surface with suction and blowing. *Appl Sci Res.* 1994;52:247–57.
 60. Sahoo A, Nandkeolyar R. Entropy generation and dissipative heat transfer analysis of mixed convective hydromagnetic flow of a Casson nanofluid with thermal radiation and Hall effect. *Sci Rep.* 2021;11:3926. <https://doi.org/10.1038/s41598-021-83124-0>.
 61. Kumar A, Tripathi R, Singh R, Sheremet MA. Entropy generation on double diffusive MHD Casson nanofluid flow with convective heat transfer and activation energy. *Indian J Phys.* 2021;91:1423–36. <https://doi.org/10.1007/s12648-020-01800-9>.

Publisher's Note Springer Nature remains neutral with regard to jurisdictional claims in published maps and institutional affiliations.